Official Journal of CIOMP
elight.springeropen.com

RESEARCH ARTICLE

Open Access

In-situ neutron-transmutation for substitutional doping in 2D layered indium selenide based phototransistor

Zhinan Guo[1†], Yonghong Zeng[1†], Fanxu Meng[1], Hengze Qu[2], Shengli Zhang[2], Shipeng Hu[1], Sidi Fan[1], Haibo Zeng[2], Rui Cao[1], Paras N. Prasad[3*], Dianyuan Fan[1] and Han Zhang[1*]

Abstract

Neutron-transmutation doping (NTD) has been demonstrated for the first time in this work for substitutional introduction of tin (Sn) shallow donors into two-dimensional (2D) layered indium selenide (InSe) to manipulate electron transfer and charge carrier dynamics. Multidisciplinary study including density functional theory, transient optical absorption, and FET devices have been carried out to reveal that the field effect electron mobility of the fabricated phototransistor is increased 100-fold due to the smaller electron effective mass and longer electron life time in the Sn-doped InSe. The responsivity of the Sn-doped InSe based phototransistor is accordingly enhanced by about 50 times, being as high as 397 A/W. The results show that NTD is a highly effective and controllable doping method, possessing good compatibility with the semiconductor manufacturing process, even after device fabrication, and can be carried out without introducing any contamination, which is radically different from traditional doping methods.

Keywords: Neutron-transmutation doping, Substitutional doping, Two-dimensional materials, Phototransistor

1 Introduction

The library of two-dimensional (2D) layered materials keeps growing, from elemental 2D materials (e.g. graphene, phosphorene and tellurium, etc.) to metal chalcogenides MX_n (for n = 1, there are InSe, SnS, SnSe, etc., and for n = 2, there are MoS_2, WS_2, etc.) [1]. Different from their bulk counterparts, 2D layered materials possess novel features, like forming van der Waals heterostructures with neglecting of lattice mismatch [2, 3],extraordinary light-mass interaction [4–6], wide tunable range of bandgap [7], and strong mechanical flexibility [8, 9], which contribute to 2D materials great potential in next-generation electronics and optoelectronics devices. Doping engineering is an important and effective way to control the electronic, optical, and many other peculiar properties of 2D materials for the application in logical circuits, sensors, and optoelectronics devices [10–12]. Various methods have been employed to realize the doping effect in 2D materials, such as substitutional doping [13], charge transfer doping [14], and intercalation doping [15]. However, for these methods additional reagents have to be used during the doping process, which may bring in contaminants, and the application of the techniques is only possible at specific steps during material synthesis or device fabrication.

Neutron transmutation doping (NTD), which is a controllable in-situ substitutional doping method that utilizes the nuclear reactions of thermal neutrons with the atoms nuclei in semiconductors [16], provides a new way to intentionally dope 2D materials without any extra

†Zhinan Guo and Yonghong Zeng authors contributed equally to this work

*Correspondence: pnprasad@buffalo.edu; hzhang@szu.edu.cn

[1] Institute of Microscale Optoelectronics, International Collaborative Laboratory of 2D Materials for Optoelectronics Science and Technology, College of Physics and Optoelectronic Engineering, Shenzhen University, Shenzhen 518060, China
[3] Institute for Lasers, Photonics, and Biophotonics and Department of Chemistry, University at Buffalo, The State University of New York, Buffalo, NY 14260, USA
Full list of author information is available at the end of the article

reagents. In addition, NTD can be introduced into any step, as demanded, during the fabrication of 2D-materials-based devices even after the devices have been fabricated. The efficiency of capturing neutrons by the nuclei of lattice atoms depends on the neutron capture cross-section and relative abundance of a given isotope. NTD has been successfully developed earlier since 1975 for bulk semiconductors like Si [17], gallium phosphide (GaP) [18], indium phosphide (InP) [19] etc. In particular, it was reported in 1991 that the tin(Sn)-related shallow donors could be uniformly introduced into the bulk indium selenide (InSe) crystal by NTD [20]. Recently, InSe have been rediscovered as a kind of 2D layered material with tunable bandgap and ultrahigh mobility, near 1000 $cm^2\ V^{-1}\ s^{-1}$ at room temperature [21–24]. Meanwhile, 2D layered InSe has also been demonstrated to possess great potential in broadband and high performance photodetection [25–28]. However, the further performance improvement of the 2D layered InSe based photodetectors is limited by the low carrier density of the unintentionally doped InSe. Therefore, it would be very interesting if the performances of 2D layered InSe based photodetector could be manipulated and optimized via the "clean" method of NTD.

In this work, Sn-doping of 2D layered InSe is realized via NTD for the first time. The doping level and structure of the Sn-doped 2D layered InSe are characterized via inductively coupled plasma atomic emission spectroscopy (ICP-AES) and spherical aberration corrected transmission electron microscope (Cs-corrected TEM). Narrowing of the bandgap and higher electron mobility of Sn-doped 2D layered InSe (Sn-InSe) have been proved by theoretical calculations and microscopic transient absorption (TA) spectra. The results show a significant improvement of the transport and photoresponse performance of the InSe phototransistor after it has been doped by NTD.

2 Results and discussion

2.1 NTD treatment for 2D layered InSe

The previous research indicates that the main nuclear reaction occurring upon irradiation of InSe with neutrons focuses on ^{115}In, the indium isotope having the relative natural abundance of 95.7%, which has a very large thermal neutron capture cross-section of 199 barn [20]. The transmutation reaction of ^{115}In and thermal neutrons (Fig. 1a) can be described as:

$$^{115}_{49}\mathrm{In}(\mathrm{n},\gamma)^{116}_{49}\mathrm{In} \rightarrow {}^{116}_{50}\mathrm{Sn}\left(\beta^{-}\mathrm{decay}\right),$$

which means the unstable ^{116}In isotope is obtained from ^{115}In isotope by capturing a thermal neutron and is then transmuted into ^{116}Sn via emission of γ and β^-. As shown in Fig. 1a, some In atoms in the honeycomb lattice of InSe would transmute into Sn atoms under thermal neutron irradiation, serving as shallow donor dopants in InSe.

The doping level (N_{Sn}/N_{In}) of Sn-doped 2D layered InSe (Sn-InSe) could be optimized by the integrated flux of thermal neutrons (F_s), as shown in Table S1. The agreement of the theoretical (calculated based on the thermal neutron capture cross-section of ^{115}In and the F_s) and experimental results (obtained by a spectrochemical method) prove that the NTD method can be theoretically predicted and precisely controlled. When the F_s was $4.32 \times 10^{17}\ cm^{-2}$, the Sn concentration of 0.008% would be obtained, indicating the InSe has been heavily doped. Sn-InSe with 0.008% Sn was used for the following experiments.

2.2 Basic characterizations of 2D layered InSe after NTD

As depicted in Additional file 1: Fig S1, the morphology of InSe after irradiation does not change significantly, indicating that InSe can maintain its morphology well under neutron irradiation. Besides, high-angle annular dark-field scanning transmission electron microscopy (HAADF-STEM) has been used to examine the changes of the crystal structure of 2D layered InSe after it has been treated by thermal neutrons irradiation, and the image of the Sn-InSe is shown in Fig. 1b. No dislocation has been observed in the image, indicating that thermal neutrons would dope the 2D layered InSe without changing its crystalline structure or bringing in any lattice defects. Atomic column intensities can be distinguished in the intensity line profile (Fig. 1c) extracted from the red dashed rectangle region marked in Fig. 1b. They are labeled as X1 (green circle), X2 (blue circle), X3 (purple circle), and X4 (orange circle), respectively. The atomic column intensities from X2 to X4 are expected to be subsequently occupied by the single Se atoms, the single In atoms, and the superposition of both In and Se atoms [29]. The higher intensity of X1 than that of X4 in the periodic array can be attributed to the superposition of both In and Se atoms with Sn dopant. It indicates the formation of substitutional Sn dopants, which is schematically shown in Additional file 1: Fig. S2. The Raman spectrum (Fig. 1d) is another evidence to show that the crystal structure remains the same after 2D layered InSe has been treated by thermal neutrons irradiation. Three dominant peaks at 114.7, 177.2, and 226.2 cm^{-1} for the 2D layered InSe samples which have been observed both before or after irradiation are ascribed to the A1 g1, E2 g1, and A1 g2 vibrational modes of InSe, respectively [29]. No shift of any peak suggests that the concentration of Sn dopants is below the detection limit of our Raman spectrometer.

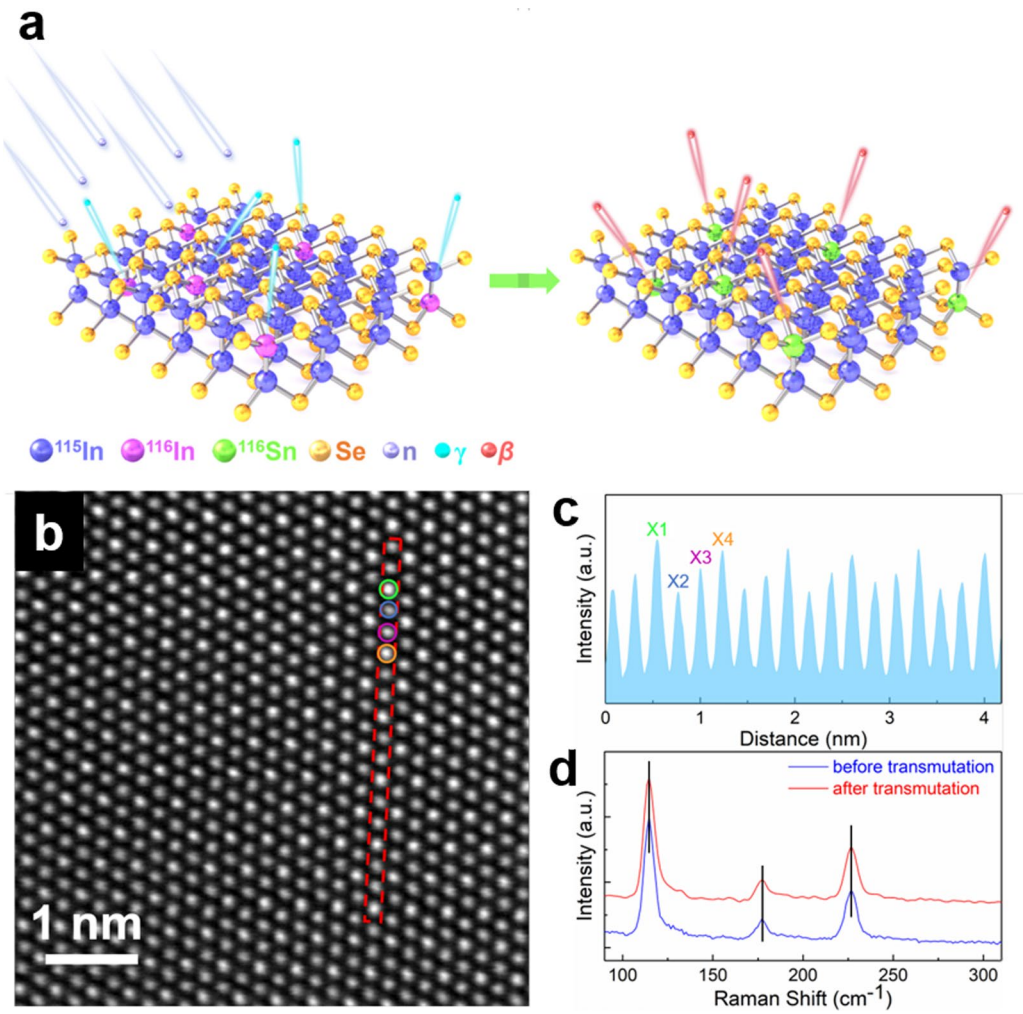

Fig. 1 The schematic of the neutron transmutation doping of InSe and the characterizations of Sn-InSe. **a** Transmutation doping scheme for the 2D layered InSe, including the capture of thermal neutrons and decay of γ and β^- particles. **b** Atomic-resolution HAADF-STEM image of the Sn-InSe. **c** The intensity profile taken from the red dashed line marked in **b**. **d** Raman spectrum (excited by 532 nm laser) of 2D layered InSe sample before and after transmutation

Temporally (0–7300 ps) and spectrally (475–770 nm) resolved microscope transient absorption (TA) spectra were used to bring insight into the NTD-induced change in the energy band structure of 2D layered InSe. As show in Fig. 2a, d, obvious red shifts could be observed at both the ground state bleaching (GSB) and excited state absorption (ESA) peaks after 2D layered InSe has been treated by thermal neutron irradiation, indicating a narrowed bandgap of 2D layered InSe and a shift of the absorption edge of Sn-InSe to longer wavelengths due to heavy doping of Sn. The ultrafast carrier dynamics of both InSe (Fig. 2b, c) and Sn-InSe (Fig. 2e, f) are shown, which were collected at two probe wavelengths, 532 nm and 655 nm (the same wavelengths were also used in the later photoresponse performance tests) with a resolution of ~ 200 fs. Two decays can be extracted from the data at 532 nm by curve fitting, where the faster one dominates. Different from the case at 532 nm, the curves at 655 nm can be well fitted by a single-exponential function. Worth noting is that each component of the fitted lifetime of carriers is increased after InSe has been irradiated by thermal neutrons. The increased carrier lifetime will contribute to the improvement of the carrier mobility, which would at the same time lead to an increased photocurrent of the 2D layered InSe based photodetector.

2.3 Theoretical simulation of intrinsic and Sn-doped 2D InSe

The changes in the electronic structures and properties of InSe and Sn-InSe have been simulated through the

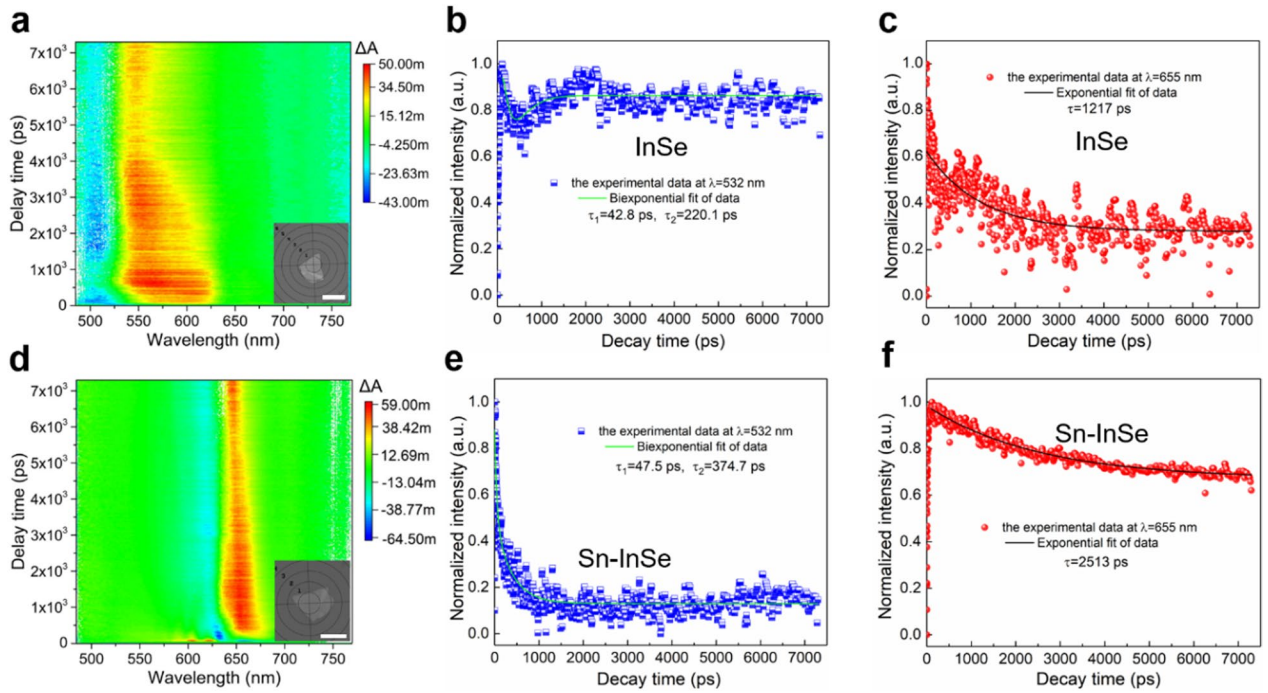

Fig. 2 Microscopic TA spectroscopy of 2D layered InSe before and after transmutation. **a**, **d** Temporally (0–7300 ps) and spectrally (475–770 nm) resolved TA signals of the 2D layered InSe (**a**) before and (**d**) after transmutation. Insets are the optical images of the samples (the scale bar is 20 μm). **b**, **c**, **e**, **f** The kinetic signals at 532 nm (**b**) and 655 nm (**c**) for the case of 2D layered InSe before transmutation and the kinetic signals at 532 nm (**e**) and 655 nm (**f**) for the case of 2D layered InSe after transmutation

density functional theory (DFT) calculations for a better understanding of the impact of NTD-induced Sn dopants on Sn-InSe. As shown in Fig. 3a, c, after one In atom has been substituted by a Sn atom, the charge density of the Sn atom mainly contributes to the Sn-In bonds in Sn-InSe. The electronic band structures of three-layer InSe and Sn-InSe are shown in Fig. 3b, d. The indirect band gap of intrinsic InSe is 1.22 eV, but for Sn-InSe, the band gap decreases to 0.61 eV, which explains the obvious red shifts in both the GSB and ESA peaks as discussed above. It also can be obtained from the calculations that the electron effective mass (m*e) of Sn-InSe (0.13 m_0) is smaller than that of the intrinsic InSe (0.21 m_0). In this case, a higher electron mobility and an enhanced photoresponse performance can be predicted from the calculated smaller m* e and longer carrier lifetime observed in TA spectra.

2.4 Transport and photoresponse performances of the 2D InSe before and after transmutation

The resistivity (ρ) measurement has been carried out by a van der Pauw method on a 2D layered InSe in 24.5 nm thickness (Additional file 1: Fig. S3). After it has been treated by thermal neutrons, the ρ of the sample decreases from 36.3 Ω·cm to 0.257 Ω·cm indicating increased electron density induced by Sn shallow donors. This is in accordance with the prediction of theoretical calculation. The transport and photoresponse performances of the same 2D InSe sample before and after transmutation were further investigated by using a back-gated field effect transistor (FET) configuration, as schematically illustrated in Fig. 4a. The thickness of the InSe sheets, the optical image of which is shown in Additional file 1: Fig. S4a, is determined by atomic force microscopy (AFM) to be ~26 nm, corresponding to ~30 layers (inset of Additional file 1: Fig. S4b). As shown in Fig. 4b, the transfer characteristics (I_{ds}-V_g) at $V_{ds} = 0.1$ V of the transmutation-doped 2D layered InSe FET exhibit a typical n-type conduction behavior with an on/off current modulation of 7.46×10^5, which is higher than that (2.54×10^5) of the nonirradiated devices. The calculated field effect electron mobility (μ_F) is also significantly improved by two orders from 1.92 to 195 $cm^2\ V^{-1}\ s^{-1}$. Besides, as shown in Additional file 1: Fig. S5c, the Hall mobility (μ_H) of the InSe before and after transmutation is 45 and 213.75 $cm^2\ V^{-1}\ s^{-1}$, respectively. Meanwhile, the carrier concentration of the transmutation-doped InSe sample is accordingly enhanced by about one order of magnitude, being as high as $2.04 \times 10^{17}\ cm^{-3}$ (Additional file 1: Fig.

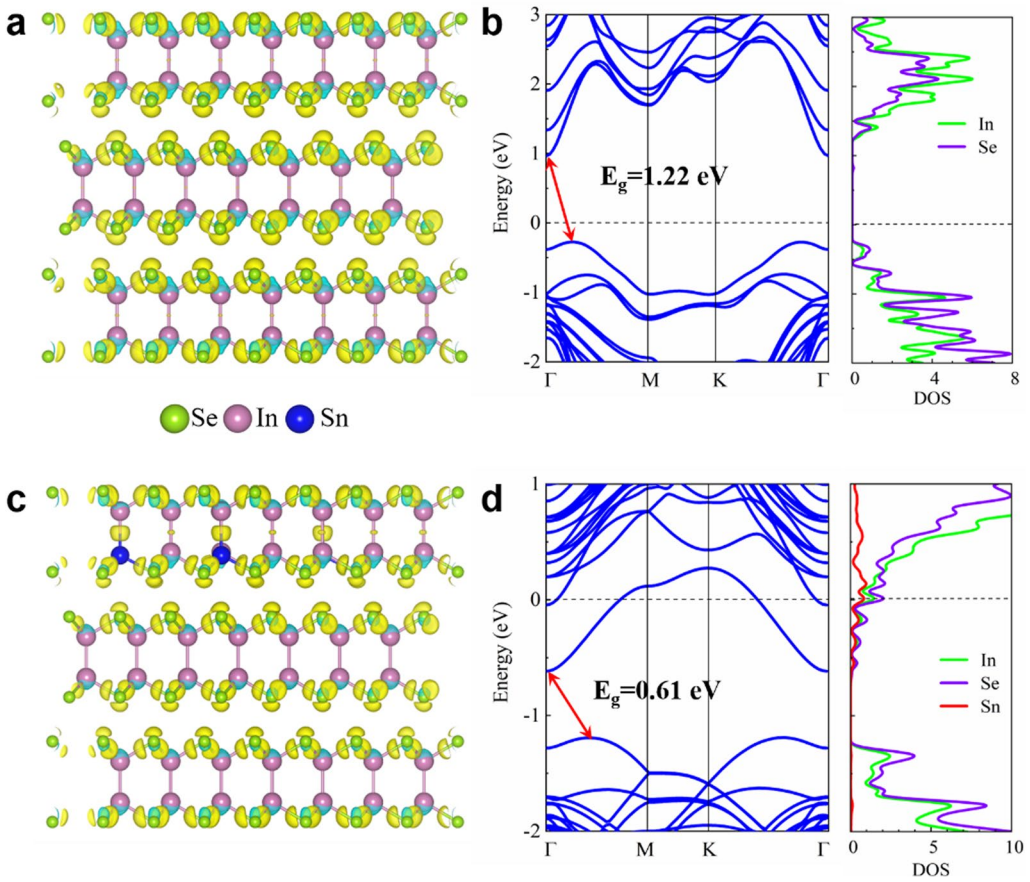

Fig. 3 DFT calculations of the charge density and band structure of intrinsic and Sn-doped 2D InSe. **a**, **b** The differential charge density (**a**) and the band structure and partial density of states (**b**) of intrinsic 2D InSe. **c**, **d** The differential charge density (**c**) and the band structure and partial density of states (**d**) of Sn-doped 2D InSe. The Fermi level is set to be 0 eV. The yellow and cyan areas in a, c represent charge accumulation and depletion, respectively

S5d). These are consistent with the prediction from DFT calculation and TA spectra.

For the photoresponse performance, the drain-source current I_{ds} at $V_g = 0$ V (see Additional file 1: Fig. S6) of the transmutation-doped 2D layered InSe FET is found to be about 2 orders higher than that of the nonirradiated devices under the illumination with each laser at the same intensity. Correspondingly, significant improvements in the responsivity (R) (Fig. 4c), external quantum efficiency (EQE) (see Additional file 1: Fig. S7a) and specific detectivity (D^*) (see Additional file 1: Fig. S7b) of the device have been observed after it has been transmutation doped. The R and D^* reach their maximum to be 397 A/W and 2.89×10^{11} Jones respectively under the illumination of a 405 nm laser. Besides, there is an increase of EQE from 42.6% to 3067.5% at 1064 nm, suggesting the red shift of InSe's absorption edge. Figure 4d shows the time-resolved photocurrent measurements of the 2D layered InSe device under different wavelengths illumination before and after it has been irradiated by thermal neutrons. The shorter rise time of the transmutation-doped device is mainly attributed to the greater electron mobility in Sn-doped InSe. However, the prolonged fall time of the device after transmutation doping is coming from a longer carrier lifetime, which is in accordance with the formerly presented microscopic TA spectra. In addition, the current can be reproducibly switched from the "on" state to the "off" state by periodically turning the light on and off (see Additional file 1: Fig. S8), which indicates a good reproducibility of the device. It is worth mentioning that a response at 1064 nm is activated only after neutron irradiation, which is attributed to the Sn-induced narrowed bandgap of InSe, which is another evidence for a red shift of the InSe's absorption edge from 1016 to 1127 nm as revealed by the DFT calculations.

In addition, we also performed the NTD experiments on some other 2D layered materials, such as graphene, black phosphorous (BP), and molybdenum disulfide

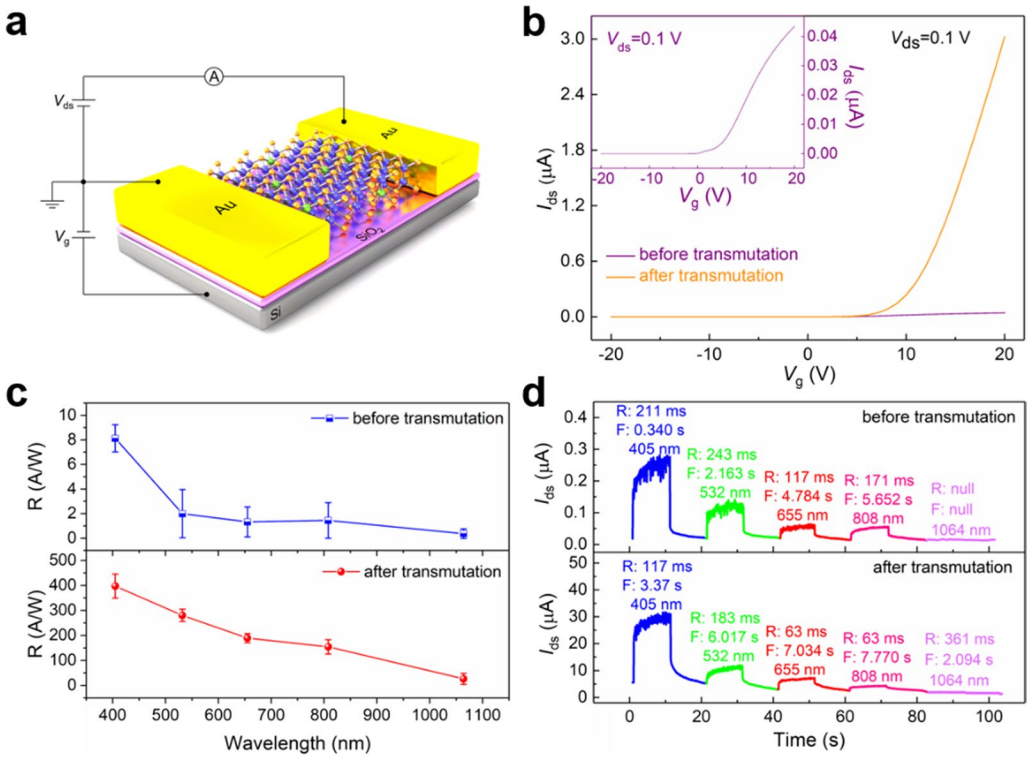

Fig. 4 Electrical characteristics and photoresponse of the 2D layered InSe FET before and after transmutation. **a** Scheme for the 2D layered InSe FET. **b** Transfer characteristics of the device before and after transmutation, with $V_{ds} = 0.1$ V. Inset is the zoom in the image of the transfer curve before transmutation. **c** The responsivity at 1 V bias of the devices before and after transmutation under the illumination of lasers at different wavelengths (405, 532, 655, 808, and 1064 nm) with the intensity of 102 mW cm^{-2}. **d** Time response (R: rise time, F: fall time) of the device before and after transmutation at 1 V bias illuminated by the pulse signal at various wavelengths

(MoS_2). Unfortunately, no similar improvement of the optoelectronics properties as in the case of InSe has been observed. This is attributed to the limited integrated flux of thermal neutrons, and small capture cross-section of these elements as shown in Additional file 1: Table S2, or the instability of the materials (Additional file 1: Fig. S9).

3 Conclusion

In summary, NTD has been successfully employed to precisely dope 2D layered InSe with Sn shallow donors without using any additional reagent, leading to a narrowed bandgap and prolonged carrier lifetime. The field effect electron mobility of 2D layered InSe FET is significantly increased from 1.92 to 195 $cm^2\ V^{-1}\ s^{-1}$ after it has been treated by thermal neutrons. Consequently, the responsivity of the photodetector is improved by about 50 times to 397 A/W and specific detectivity is increased by one order to 2.89×10^{11} Jones at 405 nm. Moreover, the device also exhibits a broadband response from visible to near infrared because of a narrower band gap produced by NTD heavy-doping.

NTD holds great promise in future materials research, enabling new material-based technologies. Examples of some strong merits from the device technologies perspective are:

(1) In the NTD method, the concentration of a dopant can be precisely estimated by the nuclear reaction formula of NTD and controlled by integrated flux of thermal neutrons.
(2) Substitutional doping can be carried out even after the accomplishment of device fabrication, which is different from traditional doping methods.
(3) The NTD method allows for doping at atomic level as well as for nano-patterned doping, when someday in future neutron beam can be controllably focused like in electron beam lithography.
(4) The NTD method would allow for the first time. A fundamental study of in-situ gradual doping effect on the carrier behavior, band structure, energy transfer etc. of 2D materials.
(5) The NTD method could be applied in sensor technology where an FET device structure with a con-

trolled optimized doping level can serve as a highly suitable platform for detection of gases as well as biological species. In addition, NTD doping can also be used for building a neutron sensor, if the 2D materials contain elements with high neutron capture cross-section, like indium (In, capture cross-section 199), tungsten (W, capture cross-section 37) or rhenium (Re, capture cross-section 74).

4 Methods

4.1 Devices fabrication

For both the 4-probe test and FET devices, 2D layered InSe samples were exfoliated from a bulk InSe crystal using Scotch tape and transferred onto a Si substrate coated with 285 nm SiO_2 by PDMS stamps. The thickness of the samples was firstly determined and chosen by the color observed via optical microscope. Au electrodes were patterned by e-beam lithography (RAITH Pioneer Two), followed by subsequently e-beam deposition of 10 nm Chromium (Cr) and 60 nm Au in a high vacuum chamber (4×10^{-6} Torr). Lift off was performed at room temperature using acetone, followed by rinse with isopropyl alcohol and nitrogen drying. The effective area of the FET devices is 57 μm^2 calculated from the optical microscopic image of the devices.

4.2 Characterization and measurements

The optical images of the samples and devices were taken by a high-resolution microscope (Olympus BX3M-LEDR). Transmission electron microscopy (TEM) and high angle annular dark field scanning TEM (HAADF-STEM) were performed on a FEI Titan Cubed Themis G2 300 transmission electron microscope equipped with energy dispersive x-ray spectroscopy (EDS) signal detector. Inductively coupled plasma atomic emission spectroscopy (ICP-AES) was performed to quantitatively analysis the relative concentration of transmuted Sn (N_{Sn}/N_{In}). The Raman data were obtained via a Horiba Jobin–Yvon LabRam HR-vis high-resolution confocal Raman microscope equipped with a 532 nm laser as the excitation source and an XYZ motorized sample stage controlled by LabSpec software. Pump–probe technique was utilized to study the carrier dynamics via transient absorption (TA) spectrometer. A mode-locked Ti:sapphire laser (Spectra Physics, Tsunami) delivered laser pulses at 800 nm and then divided into two components by means of a 9:1 beam splitter. The major component as pump light was sent to an optical parametric amplifier (OPA, TPR-TOPAS-U, America) to generate the 400 nm (1.2 mW) pump pulse. The remaining component was sent into a CaF_2 crystal and generated the visible probe pulse (475–770 nm). The delay time between pump pulse and probe pulse can be automatic adjusted through a delay device controlled by the computer with temporal resolution of 200 fs. Eventually, probe light through the sample were detected by a CMOS linear image sensor. All the transient absorption measurements were carried out at room temperature. Atomic Force Microscope (AFM, BRUKER DIMEWSION) and stylus profiler (Dektak XT, BRUKER) were performed to measure the samples' and devices' surface topographic morphology and thickness.

4-probe and FET measurements were carried out using a semiconductor characterization system (Keithley 4200) at room temperature. The devices were illuminated by 405, 532, 655, 808 and 1064 nm lasers with the same intensity of 101.86 mW cm^{-2}, respectively. For the time-resolved photocurrent measurements, a Ø1/2″ beam shutter (≤4.08 ms close activation time, SH05, THORLABS) was employed to transform the continuous lasers into pulse signals.

Hall mobility and carrier concentration of the InSe was conducted with a Hall Effect Measurement System (Bio Rad, HL5500 PC) at room temperature via van der Pauw method.

4.3 Neutron transmutation doping of 2D layered InSe samples and devices

The prepared 2D InSe samples and devices on SiO_2/Si wafers, which had been fully characterized and measured, and bulk InSe crystal were packaged into a vacuum loader. The vacuum loader was customized as shown in Additional file 1: Fig. S10. The samples were irradiated at a temperature no higher than 70 °C in vertical channels of the active zone of a VVR-ts water-cooled and water-moderated reactor, with the flux density of thermal neutrons being $\phi_s = 1 \times 10^{12}$ cm^{-2} s^{-1} for 5 days. After irradiation, the devices and samples were taken out of the vacuum loader after passing the radiation monitoring step for further characterization and measurements.

The relative concentration of transmuted Sn can be calculated with the formula [19]:

$$N_{Sn} = N_{In} k \sigma F_s,$$

where N_{Sn} is the concentration of Sn atom, N_{In} is the total number of In isotopes per unit volume, k is the relative natural abundance of ^{115}In, σ is the thermal neutron capture cross-section of ^{115}In, and F_s is the integrated flux of thermal neutrons.

4.4 Computational method of DFT

Density functional theory (DFT) calculations are performed through Vienna Ab-initio Simulation Package (VASP) code [30]. Exchange and correlation interactions are treated by generalized gradient approximation (GGA) using the Perdew-Burke-Ernzerhof (PBE)

function [31, 32]. The van der Waals interactions are treated using DFT-D2 approach of Grimme. The energy cutoff for the plane-wave basis is set as 500 eV. The convergence criterion is set to 1.0×10^{-4} eV for energy and 0.02 eV/Å for the force in each direction. A vacuum space of 30 Å is applied along z direction to avoid the any interaction between periodic images. Two Monkhorst–Pack k-point mesh of $7 \times 7 \times 1$ is adopted to sample the first Brillouin zone for 2D InSe.

Supplementary Information

The online version contains supplementary material available at https://doi.org/10.1186/s43593-022-00017-z.

Additional file 1: Table S1: Atomic percentage ratio of N_{Sn} to N_{In} obtained by inductively coupled plasma atomic emission spectroscopy (ICP-AES) and by calculation. **Figure S1**: The optical images of InSe before and after transmutation. **Figure S2**: Schematic of the few layered InSe crystal structure. **Figure S3**: 4-probe test of 2D layered InSe samples. **Figure S4**: Atomic force microscope (AFM) test of the InSe phototransistor. **Figure S5**: Hall measurement of the 2D layered InSe samples. **Figure S6**: Output characteristics of the 2D layered InSe device before and after transmutation in dark and under the illumination of lasers at different wavelengths (405, 532, 655, 808, and 1064nm) with the intensity of 101.86 mW cm^{-2}. **Figure S7**: External quantum efficiency (EQE) and specific detectivity (D^*) of the 2D layered InSe devices before and after transmutation. **Figure S8**: Periodic response of the device before and after transmutation illuminated by a pulse signal at various wavelengths. **Table S2**: Natural abundance and thermal neutron cross-section for the isotopes of C, P, S, Se, Mo, and In elements. **Figure S9**: Effect of neutron beam on some other 2D materials. **Figure S10**: Vacuum loader with samples for neutron irradiation.

Acknowledgements
The authors acknowledge the equipment the Photonics Center of Shenzhen University for technical support.

Author contributions
ZG conceived the idea and designed the experiments. ZG, YZ, HQ, SZ, SH and RC performed the main fabrication, experimental measurements, and data analysis. FM, SZ, SH, SF, HZh and PP assisted with data analysis and interpretation. ZG, YZ and FM drafted the paper and HZe, HZh, PP and DF provided revisions. All authors read and approved the final manuscript.

Funding
This work was supported by the State Key Research Development Program of China (Grant No. 2019YFB2203503), National Natural Science Fund (Grant Nos. 61875138, 61961136001, 62104153, 62105211 and U1801254), Natural Science Foundation of Guangdong Province (2018B030306038 and 2020A1515110373), Science and Technology Innovation Commission of Shenzhen (JCYJ20180507182047316 and 20200805132016001) and Postdoctoral Science Foundation of China (No.2021M702237).

Availability of data and materials
The datasets used and/or analyzed during the current study are available from the corresponding author on reasonable request.

Declarations

Competing interests
The authors declare that they have no conflict of interest.

Author details
[1]Institute of Microscale Optoelectronics, International Collaborative Laboratory of 2D Materials for Optoelectronics Science and Technology, College of Physics and Optoelectronic Engineering, Shenzhen University, Shenzhen 518060, China. [2]MIIT Key Laboratory of Advanced Display Materials and Devices, College of Material Science and Engineering, Nanjing University of Science and Technology, Nanjing 210094, China. [3]Institute for Lasers, Photonics, and Biophotonics and Department of Chemistry, University at Buffalo, The State University of New York, Buffalo, NY 14260, USA.

Received: 4 March 2022 Revised: 10 April 2022 Accepted: 18 April 2022
Published online: 06 June 2022

References

1. F. Wang et al., 2D library beyond graphene and transition metal dichalcogenides: a focus on photodetection. Chem. Soc. Rev. **47**, 6296–6341 (2018)
2. K.S. Novoselov, A. Mishchenko, A. Carvalho, A.H. Castro Neto, 2D materials and van der Waals heterostructures. Science, **353** (2016).
3. A.K. Geim, I.V. Grigorieva, Van der Waals heterostructures. Nature **499**, 419–425 (2013)
4. F.H.L. Koppens et al., Photodetectors based on graphene, other two-dimensional materials and hybrid systems. Nat. Nanotechnol **9**, 780–793 (2014)
5. S. Lukman et al., High oscillator strength interlayer excitons in two-dimensional heterostructures for mid-infrared photodetection. Nat. Nanotechnol **15**, 675–682 (2020)
6. W. Jiang et al., A versatile photodetector assisted by photovoltaic and bolometric effects. Light Sci. Appl **9**, 160 (2020)
7. Z. Qiu et al., Giant gate-tunable bandgap renormalization and excitonic effects in a 2D semiconductor. Sci. Adv **5**, eaaw2347 (2019)
8. D. Akinwande, N. Petrone, J. Hone, Two-dimensional flexible nanoelectronics. Nat Commun **5**, 5678 (2014)
9. Z. Peng, X. Chen, Y. Fan, D.J. Srolovitz, D. Lei, Strain engineering of 2D semiconductors and graphene: from strain fields to band–structure tuning and photonic applications. Light Sci. Appl **9**, 190 (2020)
10. J. Wan et al., Tuning two-dimensional nanomaterials by intercalation: materials, properties and applications. Chem. Soc. Rev **45**, 6742–6765 (2016)
11. X. Zong et al., Black phosphorus-based van der Waals heterostructures for mid-infrared light-emission applications. Light Sci. Appl **9**, 114 (2020)
12. J. Chen, Y. Xiong, F. Xu, Y. Lu, Silica optical fiber integrated with two-dimensional materials: towards opto-electro-mechanical technology. Light Sci. Appl **10**, 78 (2021)
13. F. Zhang et al., Carbon doping of WS2 monolayers: Bandgap reduction and p-type doping transport. Sci. Adv **5**, eaav5003 (2019)
14. D. Xiang et al., Surface transfer doping induced effective modulation on ambipolar characteristics of few-layer black phosphorus. Nat. Commun **6**, 1–8 (2015)
15. Y. Gong et al., Spatially controlled doping of two-dimensional SnS2 through intercalation for electronics. Nat. Nanotechnol **13**, 294–299 (2018)
16. I.S. Shlimak, Neutron transmutation doping in semiconductors: science and applications. Phys Solid State **41**, 716–719 (1999)
17. H.A. Herrmann, H. Herzer, Doping of silicon by neutron-irradiation. J. Electrochem. Soc. **122**, 1568–1569 (1975)
18. A. Huber, F. Kuchar, J. Casta, Neutron transmutation doping of gallium-phosphide. J. Appl. Phys **55**, 353–357 (1984)
19. N.G. Kolin, D.I. Merkurisov, S.P. Solov'ev, Electrical properties of transmutation-doped indium phosphide. Semiconductors **34**, 150–154 (2000)
20. B. Mari, A. Segura, A. Chevy, Electrical-properties of neutron-transmutation-doped InSe. Appl. Surf. Sci. **50**, 415–419 (1991)
21. G.W. Mudd et al., Tuning the bandgap of exfoliated InSe nanosheets by quantum confinement. Adv. Mater **25**, 5714–5718 (2013)
22. S. Lei et al., Evolution of the electronic band structure and efficient photo-detection in atomic layers of InSe. ACS Nano **8**, 1263–1272 (2014)
23. D.A. Bandurin et al., High electron mobility, quantum Hall effect and anomalous optical response in atomically thin InSe. Nat. Nanotechnol **12**, 223–227 (2017)
24. M. Dai et al., Robust piezo-phototronic effect in multilayer γ-InSe for high-performance self-powered flexible photodetectors. ACS Nano **13**, 7291–7299 (2019)

25. S.R. Tamalampudi et al., High performance and bendable few-layered InSe photodetectors with broad spectral response. Nano Lett **14**, 2800–2806 (2014)
26. G.W. Mudd et al., High broad-band photoresponsivity of mechanically formed InSe–graphene Van Der Waals heterostructures. Adv. Mater. **27**, 3760–3766 (2015)
27. A. Gao et al., Observation of ballistic avalanche phenomena in nanoscale vertical InSe/BP heterostructures. Nat. Nanotechnol **14**, 217–222 (2019)
28. Z. Guo et al., High performance polarization sensitive photodetectors on two-dimensional β-InSe. Natl. Sci. Rev (2021). https://doi.org/10.1093/nsr/nwab098
29. Q. Hao et al., Phase identification and strong second harmonic generation in pure ε-InSe and its alloys. Nano Lett **19**, 2634–2640 (2019)
30. G. Kresse, J. Furthmuller, Efficient iterative schemes for ab initio total-energy calculations using a plane-wave basis set. Phys. Rev. B **54**, 11169–11186 (1996)
31. J.P. Perdew, K. Burke, M. Ernzerhof, Generalized gradient approximation made simple. Phys. Rev. Lett **77**, 3865–3868 (1996)
32. P.E. Blochl, Projector augmented-wave method. Phys. Rev. B Condens Matter **50**, 17953–17979 (1994)